electronic reprint

JOURNAL OF APPLIED CRYSTALLOGRAPHY

ISSN: 1600-5767
journals.iucr.org/j

Aberration corrections for non-Bragg–Brentano diffraction geometries

Matthew R. Rowles and Craig E. Buckley

J. Appl. Cryst. (2017). **50**, 240–251

JOURNAL OF APPLIED CRYSTALLOGRAPHY

ISSN 1600-5767

Aberration corrections for non-Bragg–Brentano diffraction geometries

Matthew R. Rowles* and Craig E. Buckley

Department of Physics and Astronomy, Fuels and Energy Technology Institute, Curtin University, GPO Box U1987, Perth, Australia. *Correspondence e-mail: matthew.rowles@curtin.edu.au

Received 20 September 2016
Accepted 3 January 2017

Edited by K. Chapman, Argonne National Laboratory, USA

Keywords: fundamental parameters; Rietveld modelling; aberration corrections.

Supporting information: this article has supporting information at journals.iucr.org/j

The construction of peak intensity, profile and displacement aberration functions based on the geometry of a powder diffraction measurement allows for physically realistic corrections to be applied in Rietveld modelling through a fundamental parameters approach. Parallel-beam corrections for asymmetric reflection and Debye–Scherrer geometry are summarized, and corrections for thin-plate transmission are derived and validated. Geometrically correct implementations of preferred orientation models are also summarized.

1. Introduction

With the growth in synchrotron experimentation, the use of *in situ* techniques and the availability of multiple optical configurations for laboratory instruments, more measurements are being conducted in geometries that deviate from the *de facto* Bragg–Brentano standard. As the experimental geometry changes, so too do the ways in which aberrations arising from specimen displacement, absorption (or transparency) and preferred orientation manifest themselves in the diffraction pattern. An understanding of the data collection geometry allows for an understanding of how all of these, and other, factors differ, and how to correct for their effects in Rietveld (1969) modelling.

The construction of peak intensity, profile and displacement corrections based on the diffraction geometry through the fundamental parameters approach (Cheary & Coelho, 1992), rather than the use of empirical functions, enables physically realistic corrections to be applied in models, allowing for stronger results and conclusions to be drawn from the analysis of diffraction data. Such realistic models also allow for the direct comparison of data collected in different geometries, enabling the researcher to pursue the best instrument geometry for a particular experiment, whilst being free to use previous results from other instruments. The corrections outlined here assume a parallel beam; generalization to divergent and focused beams is beyond the scope of the current work. For a review on aberrations for Bragg–Brentano instruments, and how they can be derived and applied through the fundamental parameters approach, please refer to Cheary *et al.* (2004). Furthermore, the corrections given here refer only to equatorial aberrations; for corrections related to axial divergence, please refer to Cheary & Coelho (1998*a*,*b*), Finger *et al.* (1994) and van Laar & Yelon (1984).

2. Geometrical corrections

2.1. Flat-plate asymmetric reflection

In the case of asymmetric reflection geometry, where a parallel beam is incident on the specimen surface at a fixed

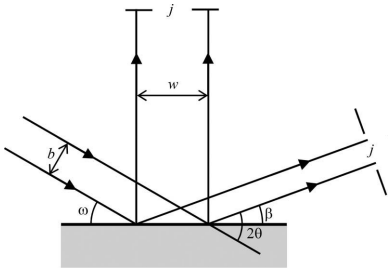

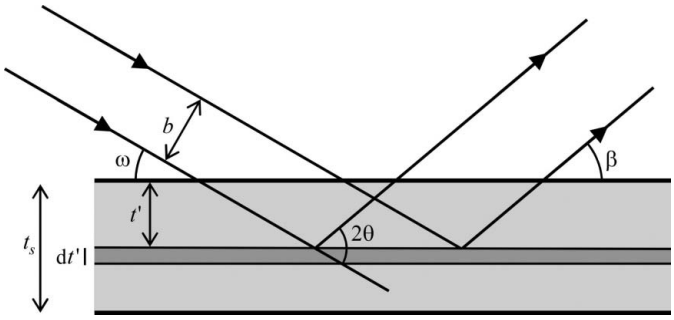

Figure 1
X-ray paths in flat-plate reflection geometry (after Egami & Billinge, 2003, p. 194). The incident and diffracted beams make an angle of ω and β, respectively, with the specimen surface. We consider an infinitesimal thickness, dt', in equation (1). The specimen thickness is t_s. $2\theta = \omega + \beta$.

angle, there are several corrections required to allow for changes in peak intensity, profile and displacement. The form of these corrections also depends on the specimen thickness.

2.1.1. Peak intensity corrections. As outlined by Egami & Billinge (2003, pp. 193–195), and shown in Fig. 1, the volume of material contributing to the diffracted intensity is given by

$$V = \frac{A}{\sin\omega}\int_0^{t_s} \exp\left[-\mu t'\left(\frac{1}{\sin\omega}+\frac{1}{\sin\beta}\right)\right]\mathrm{d}t'$$
$$= \frac{A}{\mu}\left(1+\frac{\sin\omega}{\sin\beta}\right)^{-1}\left\{1-\exp\left[-\mu t_s\left(\frac{1}{\sin\omega}+\frac{1}{\sin\beta}\right)\right]\right\}, \quad (1)$$

where A is the area of the incident X-ray beam on the specimen surface, μ is the linear absorption coefficient of the specimen, t_s is the specimen thickness, ω is the angle between the incident beam and the specimen surface, and β is the angle between the diffracted beam and the specimen surface, such that $\beta = 2\theta - \omega$.

For an infinitely thick[1] specimen in symmetric reflection, where $\omega = \beta = \theta$, this volume is simply

$$V_{\mathrm{SR}} = \frac{A}{2\mu}, \quad (2)$$

which shows the classic constant diffraction volume of symmetric reflection geometry with diffraction angle. The diffracted volume for an infinitely thick specimen in asymmetric reflection is

$$V_{\mathrm{AR}} = \frac{A}{\mu}\left(1+\frac{\sin\omega}{\sin\beta}\right)^{-1}. \quad (3)$$

As the diffracted intensity depends on the amount of material diffracting, taking the ratio of these volumes reproduces the intensity correction factor of Toraya *et al.* (1993):

$$\frac{V_{\mathrm{AR}}}{V_{\mathrm{SR}}} = I^{\mathrm{AR}}_{\mathrm{scale}} = 2\left(1+\frac{\sin\omega}{\sin\beta}\right)^{-1}. \quad (4)$$

[1] A specimen is considered infinitely thick when the exponential term in equation (1) is less than 0.01, that is, the correction is less than 1% (Zevin & Kimmel, 1995).

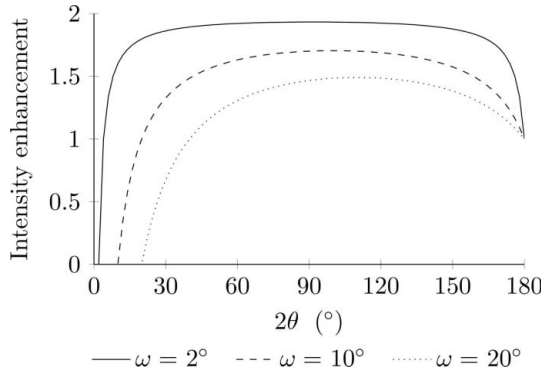

Figure 2
Intensity enhancement, with respect to symmetric reflection, for infinitely thick specimens in asymmetric reflection geometry. Three different incident angles are given. The curves in this figure are described by equation (4), with $\beta = 2\theta - \omega$.

That is, the intensities in asymmetric reflection are altered with respect to symmetric reflection by this factor. Fig. 2 shows how this factor changes with incident and diffracted angles.

If, however, the specimen cannot be considered to be infinitely thick, then the specimen thickness must be taken into

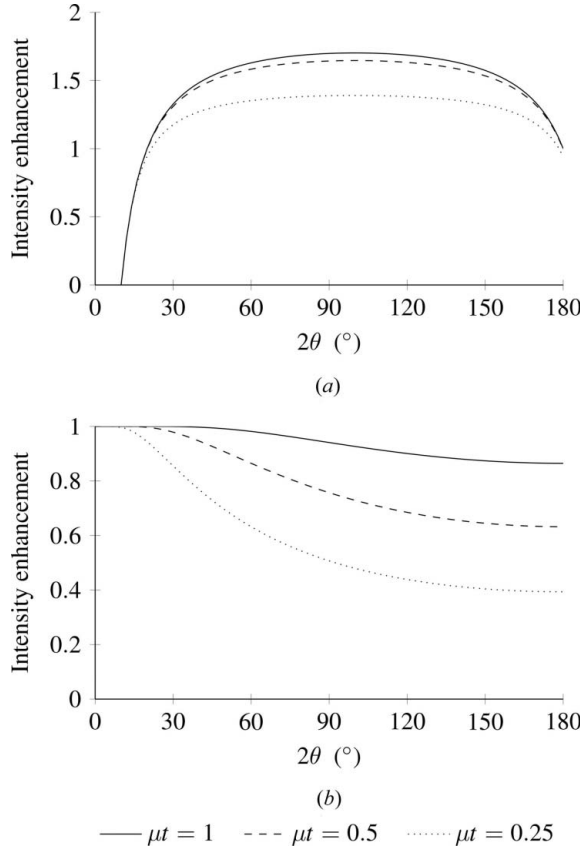

Figure 3
Intensity enhancement for thin specimens, with respect to symmetric reflection from an infinitely thick specimen, in (*a*) asymmetric ($\omega = 10°$) and (*b*) symmetric reflection geometry. If the linear absorption coefficient for the specimen was 100 cm^{-1}, then the specimen thicknesses shown would correspond to 100, 50 and 25 µm. The curves in this figure are defined by equations (5) and (6), with $\beta = 2\theta - \omega$.

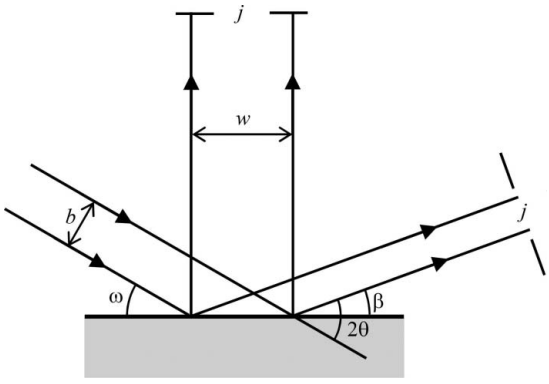

Figure 4
A schematic of the change in the width of the diffracted beam, w, and the influence of the detector slit width, j, on the measured diffracted intensity, as given in equation (8). In the case of a position-sensitive detector, the change in beam size can be modelled with a hat convolution (Rowles & Madsen, 2010) [see equation (18)].

account, and the relevant intensity correction factor in asymmetric reflection, shown in Fig. 3(*a*), becomes

$$I_{\rm scale}^{\rm AR} = 2\left(1+\frac{\sin\omega}{\sin\beta}\right)^{-1}\left\{1-\exp\left[-\mu t_{\rm s}\left(\frac{1}{\sin\omega}+\frac{1}{\sin\beta}\right)\right]\right\}, \tag{5}$$

with an equivalent correction for symmetric reflection, shown in Fig. 3(*b*), of

$$I_{\rm scale}^{\rm SR} = 1-\exp\left(-\mu t_{\rm s}\frac{2}{\sin\theta}\right). \tag{6}$$

Extending the application of thin layers further to multilayer materials, then the intensity from the buried layers must be reduced owing to the fact that the incident and diffracted beams pass through the surface layers to the layer of interest. To that end, for each layer that the X-rays must travel through, the intensity must be scaled by a factor

$$I_{\rm scale} = \exp\left[-\mu t\left(\frac{1}{\sin\omega}+\frac{1}{\sin\beta}\right)\right], \tag{7}$$

where μ and t are the linear absorption coefficient and layer thickness, respectively, of the layer immediately above the layer of interest. This factor accounts for the intensity loss in both the incident and diffracted beams. Furthermore, the peak positions from the buried layers must be corrected to account for their displacement from the centre of the goniometer [see equations (19) and (20)].

For point detectors, the detected diffracted intensity is affected by the detector slit width, j. If the diffracted beam is smaller than this value, then the entire diffracted beam is counted. Once the beam grows beyond this width, as shown in Fig. 4, then the detected intensity drops off (Toraya *et al.*, 1993) and can be accounted for by the correction

$$I_{\rm scale} = {\rm Min}\left(1, \frac{j}{b}\frac{\sin\omega}{\sin\beta}\right), \tag{8}$$

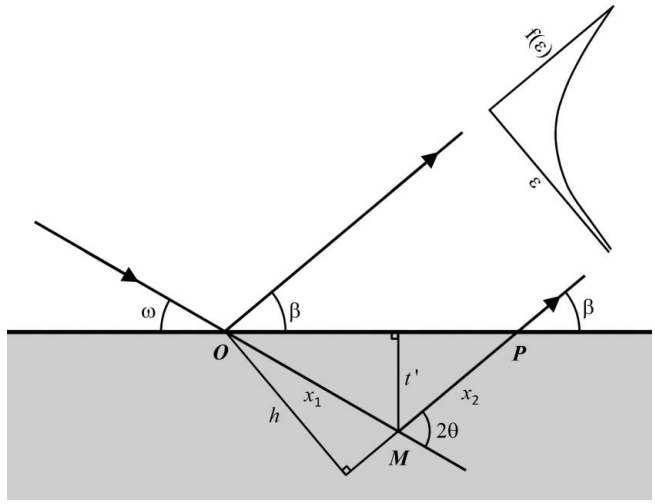

Figure 5
Geometrical construction of the absorption aberration correction for reflection geometry. The path lengths of the incident and diffracted beams through the specimen are given by x_1 and x_2, respectively. ε can be approximated by $-h/R_{\rm s}$, where $R_{\rm s}$ is the specimen–detector distance. The aberration correction, $f(\varepsilon)$, is given in equation (13). Figs. 6 and 7 show the effect of diffraction angle, linear absorption coefficient and specimen thickness.

where Min(x, y) chooses the smallest value of x or y, j is the detector slit width, and b is the incident beam height.

2.1.2. Peak profile corrections. The diffraction peak profiles also change with the change in geometry, because of absorption,[2] and can be modelled as an exponential aberration. Following the derivation of Masson *et al.* (1996), Fig. 5 shows that the path length of the X-ray beam through the specimen is given by $x = x_1 + x_2$, where

$$t' = h\frac{\sin\omega}{\sin 2\theta}, \tag{9}$$

$$x_1 = \frac{t'}{\sin\omega}, \tag{10}$$

$$x_2 = \frac{t'}{\sin\beta}. \tag{11}$$

The intensity of the beam emerging at P, with respect to O, diffracted at M, is reduced by a factor of $\exp(-\mu x)$. Given that the specimen–detector distance is $R_{\rm s}$, then $h/R_{\rm s}$ is a small value, and the angular variable $\varepsilon = 2\theta' - 2\theta$, where $2\theta'$ is the angle at which diffraction is observed and 2θ is the angle at which diffraction occurs, can be approximated as

$$\varepsilon = -\frac{h}{R_{\rm s}}\frac{180}{\pi} \tag{12}$$

in degrees. Substituting equations (9)–(12) into a normalized exponential with $-\mu x = \varepsilon/\delta$, the profile change induced by specimen absorption is given by

$$f(\varepsilon) = \begin{cases} (1/\delta)\exp(\varepsilon/\delta) & \varepsilon \le 0 \\ 0 & \text{otherwise} \end{cases} \tag{13}$$

[2] Also known as transparency. As absorption decreases, the transparency increases, and a correction becomes necessary.

where

$$\delta = \left[\mu R_s \frac{1}{\sin 2\theta}\left(1 + \frac{\sin\omega}{\sin\beta}\right)\right]^{-1} \frac{180}{\pi} \tag{14}$$

and is applicable to a specimen of infinite thickness. This is equivalent to the expression given by Masson *et al.* (1996). Fig. 6 shows the absorption profile for a range of linear absorption coefficients at 30 and 90° 2θ.

For thin specimens, the cessation of the layer will also truncate the absorption profile. In order to model this, the range of the aberration correction must be limited to a minimum value where

$$h_{\max} = t_s \frac{\sin 2\theta}{\sin\omega} \tag{15}$$

is substituted into equation (12) to find the lower limit to ε,

$$\varepsilon_{\min} = -\frac{t_s}{R_s}\frac{\sin 2\theta}{\sin\omega}\frac{180}{\pi}, \tag{16}$$

such that

$$f(\varepsilon) = \begin{cases} \left(1/\left\{\delta\left[1 - \exp(\varepsilon_{\min}/\delta)\right]\right\}\right)\exp(\varepsilon/\delta) & \varepsilon_{\min} \le \varepsilon \le 0 \\ 0 & \text{otherwise} \end{cases} \tag{17}$$

where t_s is the thickness of the layer, δ is defined in equation (14) and $\varepsilon_{\min}$ is defined in equation (16). The additional prefactor with respect to equation (13) is required to maintain normalization. This absorption correction can be applied to multilayer structures without alteration. Fig. 7 shows the absorption profile for a range of layer thicknesses at 30 and 90° 2θ.

If the diffractometer has no diffracted beam optics, as is the case with a large curved position-sensitive detector such as the Mythen (Schmitt *et al.*, 2003) or Inel CPS, then the peak profile is also affected by the size of the beam on the specimen. The width in degrees, w, of the diffracted beam at the detector, shown in Fig. 4, changes with diffraction angle as

$$w = \frac{b}{\sin\omega}\frac{\sin\beta}{R_s}\frac{180}{\pi}, \tag{18}$$

where b is the height of the beam and R_s is the specimen–detector distance. This change in diffracted beam width can be modelled by the inclusion of a hat convolution, or the combination of a hat + Gaussian convolution (Rowles & Madsen, 2010).

The apparent size of the beam on the detector can also be affected by the finite size of a pixel in pixel detectors. Each pixel can be considered to be analogous to a receiving slit in a

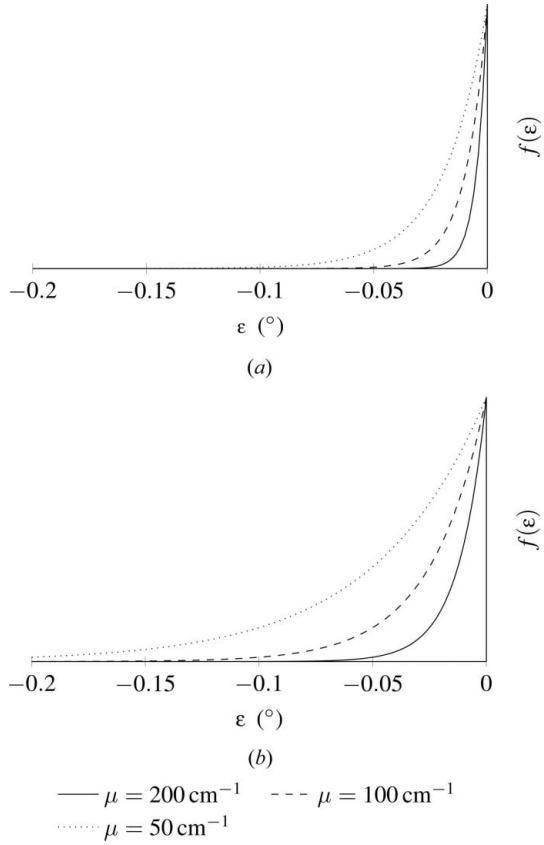

Figure 6
Normalized absorption profiles for an infinitely thick specimen in asymmetric reflection geometry at (*a*) 30 and (*b*) 90° 2θ, for a range of linear absorption coefficients. These profiles are described by equation (13) with $\omega = 10°$ and $R_s = 200$ mm, and with $\beta = 2\theta - \omega$.

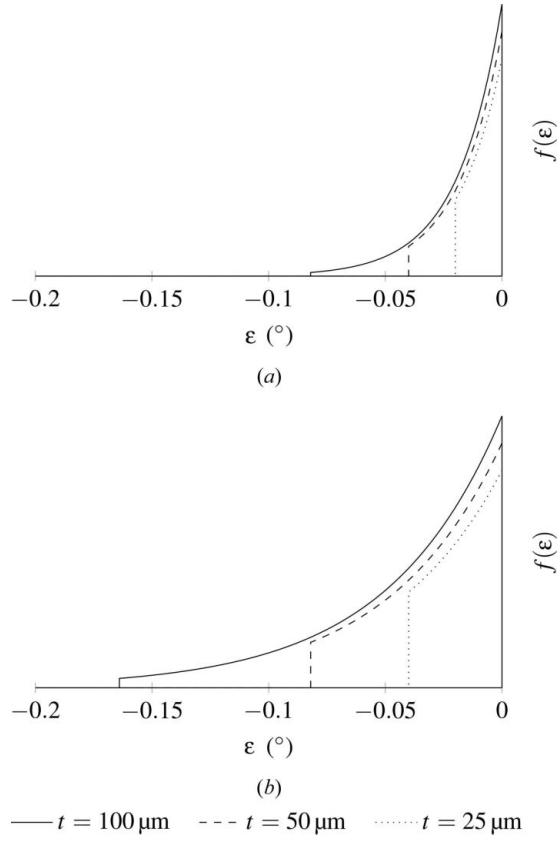

Figure 7
Normalized absorption profiles for a thin specimen in asymmetric reflection geometry at (*a*) 30 and (*b*) 90° 2θ, for a range of specimen thicknesses. The profiles have been scaled for clarity, as they are identical prior to their cutoff. These profiles are described by equation (17) with $\mu = 50$ cm^{-1}, $\omega = 10°$ and $R_s = 200$ mm, and with $\beta = 2\theta - \omega$.

conventional Bragg–Brentano instrument, and as such, the effect of finite pixels on the peak profile can be modelled as a hat function with a width given by the pixel dimensions (Cheary *et al.*, 2004). In cases of high intensity, the simple hat approximation would need to be modified to match the point-spread function of the detector.

If the diffractometer has a parallel plate collimator, also known as analyser slits or equatorial Soller slits, in the diffracted beam, then this will introduce a triangular aberration in the peaks (Cheary *et al.*, 2004). These may be modelled by simply including two hat functions with identical widths corresponding to the angular acceptance of the slits.

2.1.3. Peak position corrections. The angular dependence of peak positions due to specimen displacement is also altered with respect to the Bragg–Brentano setup, as shown in Fig. 8. Assuming a small angle, the peak offset in degrees due to a specimen displacement, s, perpendicular to the specimen surface is given by

$$\delta = \frac{s_1}{R_s}\frac{\sin 2\theta}{\sin\omega}\frac{180}{\pi} \tag{19}$$

or, if the displacement is perpendicular to the incident beam,

$$\delta = \frac{s_2}{R_s}\frac{\sin 2\theta}{\tan\omega}\frac{180}{\pi}, \tag{20}$$

where R_s is the specimen–detector distance. These different implementations may be necessary depending on how a specific instrument is designed to hold the specimen and orient it to the incident beam.

2.2. Thin flat-plate transmission

In the case of symmetric and asymmetric transmission geometry, where a parallel beam is incident on the specimen surface at some angle ω, the changes in peak intensity, profile and displacement are again different, and also depend on the specimen thickness and linear absorption coefficient.

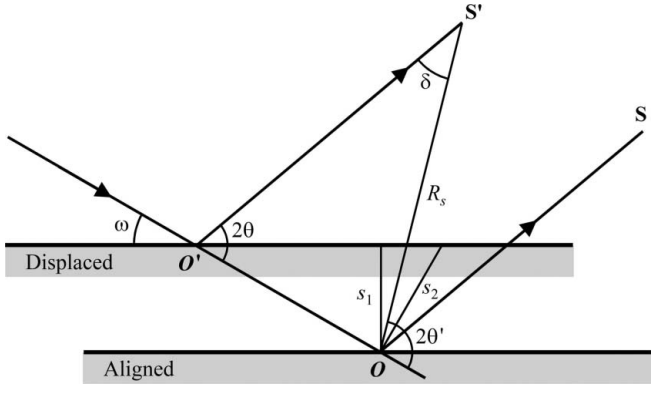

Figure 8
Geometrical argument for the specimen displacement correction for asymmetric reflection geometry. The specimen can be displaced either perpendicular to its surface (s_1) or perpendicular to the incident beam (s_2), depending on the goniometer construction. This displacement causes a diffraction peak with an angle 2θ, which should be recorded at S, to be recorded at S', with a diffraction angle of $2\theta + \delta$. R_s is the specimen–detector distance. δ is given in equations (19) and (20).

2.2.1. Peak intensity corrections. As outlined by Egami & Billinge (2003, p. 199), and shown in Fig. 9, the volume of material contributing to the diffracted intensity is given by

$$\begin{aligned} V &= \frac{A}{\sin\omega}\exp\left(-\frac{\mu t_s}{\sin\beta}\right)\int_0^{t_s}\exp\left[-\mu t'\left(\frac{1}{\sin\omega}-\frac{1}{\sin\beta}\right)\right]\mathrm{d}t' \\ &= \frac{A}{\mu}\exp\left(-\frac{\mu t_s}{\sin\beta}\right)\left(\frac{\sin\omega}{\sin\beta}-1\right)^{-1} \\ &\quad\times\left\{\exp\left[-\mu t_s\left(\frac{1}{\sin\omega}-\frac{1}{\sin\beta}\right)\right]-1\right\}, \end{aligned} \tag{21}$$

where A is the area of the incident X-ray beam on the specimen surface, μ is the linear absorption coefficient of the specimen, t_s is the specimen thickness, ω is the angle between the incident beam and the specimen surface, and β is the angle between the diffracted beam and the specimen surface, such that $\beta = 180 - (2\theta + \omega)$.

As the intensity of diffraction is proportional to this volume, the volume can be expressed as a normalized value to represent diffracted intensity, which can be taken with respect to the volume at 0° 2θ (Klug & Alexander, 1974) or, as in this paper, to the volume for symmetric reflection [equation (2)]. For a specimen in asymmetric transmission, this normalized volume, and hence the intensity scale, is given by

$$\begin{aligned} I_{\mathrm{scale}}^{\mathrm{AT}} &= 2\exp\left(-\frac{\mu t_s}{\sin\beta}\right)\left(\frac{\sin\omega}{\sin\beta}-1\right)^{-1} \\ &\quad\times\left\{\exp\left[-\mu t_s\left(\frac{1}{\sin\omega}-\frac{1}{\sin\beta}\right)\right]-1\right\}, \end{aligned} \tag{22}$$

where the difference between the two normalization methods is simply a constant factor which can be accounted for in the Rietveld scale factor. If $\omega = \beta$, this expression reduces to that

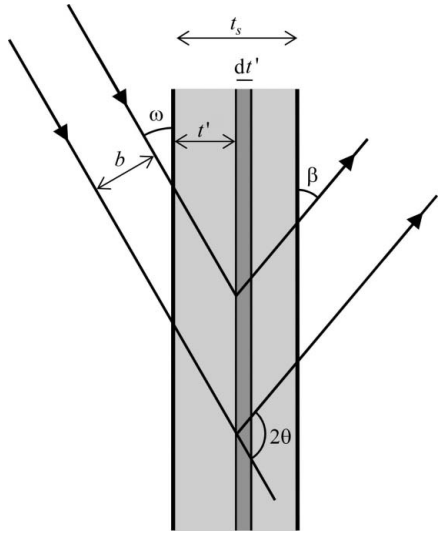

Figure 9
X-ray paths in flat-plate transmission geometry (after Egami & Billinge, 2003, p. 199). The incident and diffracted beams make an angle of ω and β, respectively, with the specimen surface. We consider an infinitesimal thickness, $\mathrm{d}t'$, in equation (21). The specimen thickness is t_s. $2\theta = 180 - (\omega + \beta)$.

given in equation (24). The variation of this correction with 2θ is shown in Figs. 10(a) and 10(b) for two different incident angles.

For a specimen in symmetric transmission, where $\omega = \beta = 90 - \theta$, the diffraction volume is simply

$$V_{\rm ST} = \frac{At_{\rm s}\exp(-\mu t_{\rm s}/\cos\theta)}{\cos\theta} \tag{23}$$

and can be normalized to the volume for symmetric reflection as outlined above, yielding

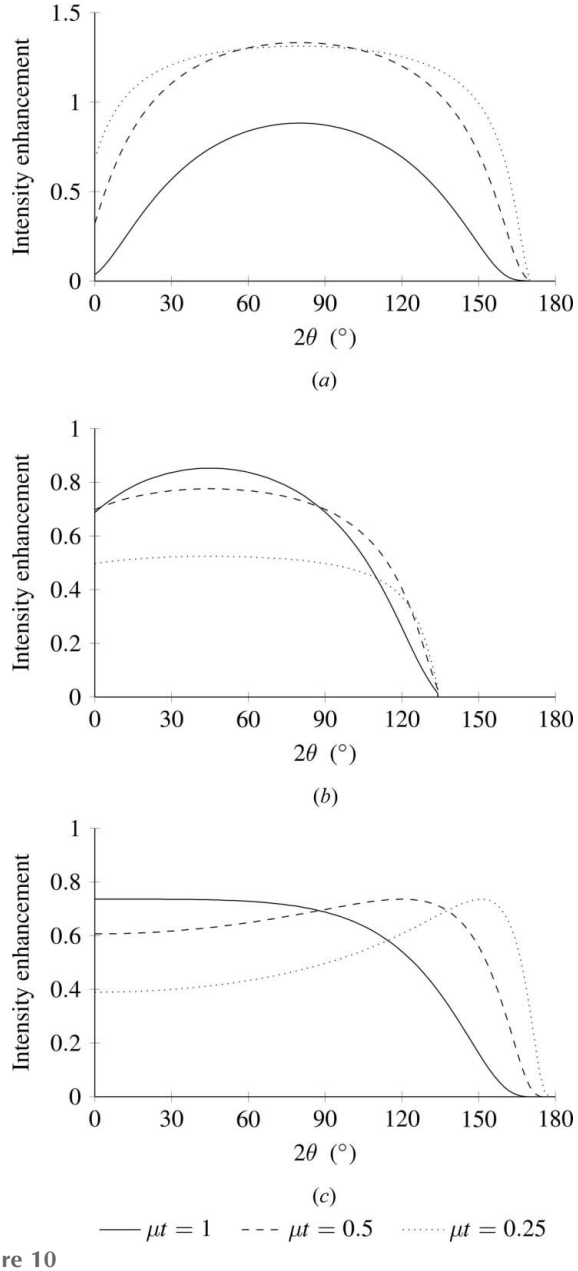

Figure 10
Intensity enhancement for thin specimens in (a) asymmetric ($\omega = 10°$), (b) asymmetric ($\omega = 45°$) and (c) symmetric transmission geometry, with respect to symmetric reflection from an infinitely thick specimen. If the linear absorption coefficient for the specimen was 100 cm^{-1}, then the specimen thicknesses shown would correspond to 100, 50 and 25 µm. These curves are produced by equations (22) and (24).

$$I_{\rm scale}^{\rm ST} = \frac{2\mu t_{\rm s}\exp(-\mu t_{\rm s}/\cos\theta)}{\cos\theta}. \tag{24}$$

The variation of this correction with 2θ is shown in Fig. 10(c).

If the specimen consists of a number of layers, then each one can be considered separately, as in reflection geometry, with separate intensity corrections and a specimen displacement correction [see equations (39) and (40)] for each layer to account for their offset from the goniometer centre. In the transmission case, the intensities for a layer must be scaled by

$$I_{\rm scale} = \exp\left(-\frac{\mu t}{\sin\omega}\right) \tag{25}$$

for each layer before the layer of interest and

$$I_{\rm scale} = \exp\left(-\frac{\mu t}{\sin\beta}\right) \tag{26}$$

for each layer after the layer of interest, where μ and t are the linear absorption coefficients and thicknesses, respectively, of each preceding and succeeding layer.

2.2.2. Peak profile corrections. The diffraction peak profiles also change as a result of absorption. Following the nomenclature of Masson *et al.* (1996), the absorption correction can be derived as follows.

Consider an infinitely thin X-ray beam incident at an angle ω at point O on the front surface of a flat specimen with a linear absorption coefficient μ, being diffracted at point M through an angle 2θ, and leaving the rear surface at point P at an angle β, where $\beta = 180 - (2\theta + \omega)$, as shown in Fig. 11. The incident and diffracted path lengths, respectively, are given by

$$x_1 = \frac{t'}{\sin\omega}, \tag{27}$$

$$x_2 = \frac{t_{\rm s} - t'}{\sin\beta}. \tag{28}$$

Here,

$$t' = h\frac{\sin\omega}{\sin 2\theta} \tag{29}$$

and h exists in the range $0 \le h \le h_{\rm max}$, where

$$h_{\rm max} = t_{\rm s}\frac{\sin 2\theta}{\sin\omega}. \tag{30}$$

By substituting equation (29) into equations (27) and (28), and calculating the total path length of the X-ray beam through the specimen as $x = x_1 + x_2$, we can show that

$$x = \frac{h}{\sin 2\theta}\left(1 - \frac{\sin\omega}{\sin\beta}\right) + \frac{t_{\rm s}}{\sin\beta}. \tag{31}$$

Given that the specimen–detector distance is $R_{\rm s}$, then $h/R_{\rm s}$ is a small value, and the angular variable $\varepsilon = 2\theta' - 2\theta$, where $2\theta'$ is the angle at which diffraction is observed and 2θ is the angle at which diffraction occurs, can be approximated as

$$\varepsilon = -\frac{h}{R_{\rm s}}\frac{180}{\pi} \tag{32}$$

in degrees; a minus sign is used as h is defined as a positive value. ε exisits in the range $\varepsilon_{\min} \leq \varepsilon \leq 0$, where $\varepsilon_{\min}$ is found by substituting equation (30) into (32) as

$$\varepsilon_{\min} = -\frac{t_s}{R_s}\frac{\sin 2\theta}{\sin \omega}\frac{180}{\pi}. \quad (33)$$

The diffracted X-ray beam is reduced in intensity by a factor $\exp(-\mu x)$ with respect to the incident beam. By substituting equations (31) and (32) into this exponential, we can find the unnormalized exponential as

$$g(\varepsilon) = \exp\left\{-\mu\left[\frac{\pi}{180}\frac{\varepsilon R_s}{\sin 2\theta}\left(\frac{\sin \omega}{\sin \beta} - 1\right) + \frac{t_s}{\sin \beta}\right]\right\}, \quad (34)$$

which can be normalized by dividing it by its integral from $\varepsilon_{\min}$ to 0,

$$N = \frac{\sin 2\theta}{\mu R_s}\left(\frac{\sin \omega}{\sin \beta} - 1\right)^{-1}\left[\exp\left(\frac{\mu t_s}{\sin \beta}\right) - \exp\left(\frac{\mu t_s}{\sin \omega}\right)\right] \times \exp\left[-\mu t_s\left(\frac{1}{\sin \omega} + \frac{1}{\sin \beta}\right)\right]\frac{180}{\pi}. \quad (35)$$

By combining equations (34) and (35) with (33), the normalized convolution for the correction of the peak profile for absorption in asymmetric transmission geometry is

$$f(\varepsilon) = \begin{cases} g(\varepsilon)/N & \varepsilon_{\min} \leq \varepsilon \leq 0 \\ 0 & \text{otherwise} \end{cases} \quad (36)$$

and Fig. 12 shows the absorption profile for a range of specimen thicknesses at 0 and 90° 2θ. If $\omega = \beta$, this expression reduces to that given in equation (37).

In the specific case of symmetric transmission, the absorption aberration correction is much simpler. Following through the same reasoning as outlined in equations (27)–(35) where $\omega = \beta = 90 - \theta$, the normalized correction is given by

$$f(\varepsilon) = \begin{cases} \dfrac{R_s}{2t_s}\dfrac{1}{\sin \theta}\dfrac{\pi}{180} & -\dfrac{2t_s}{R_s}\sin\theta\dfrac{180}{\pi} \leq \varepsilon \leq 0 \\ 0 & \text{otherwise} \end{cases} \quad (37)$$

and Fig. 13 shows the absorption profile for a range of specimen thicknesses at 30 and 90° 2θ. Owing to the geometry, the X-ray path length is now independent of ε, and the correction is simply a constant which serves to broaden the diffracted beam.

In reality, an incident beam has some height. For a parallel beam of some finite size incident on the specimen surface, its width can be accounted for by the inclusion of a peak width correction following the principles of Rowles & Madsen (2010). In this instance, the peak profile is broadened as a result of the beam height as

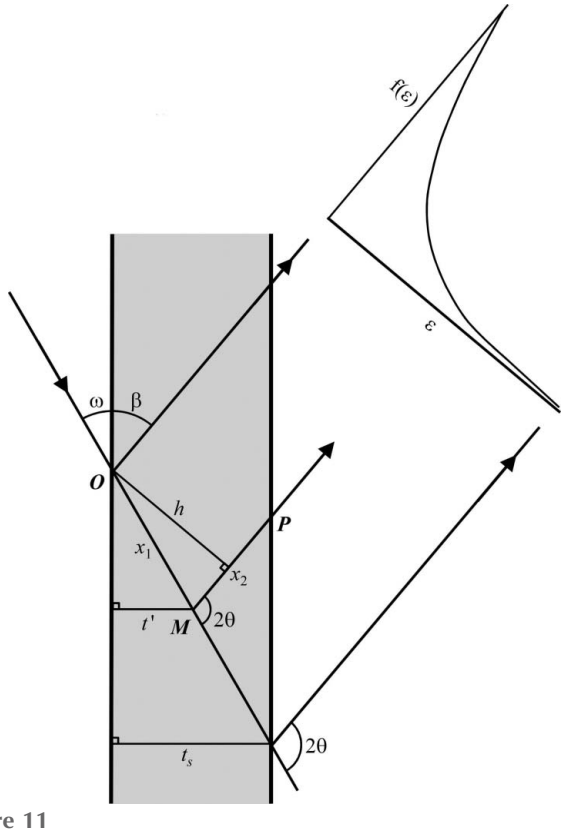

Figure 11
Geometric construction of the absorption aberration correction for flat-plate transmission geometry with a specimen thickness of t_s. The path lengths of the incident and diffracted beams through the specimen are given by x_1 and x_2, respectively. ε can be approximated by $-h/R_s$, where R_s is the specimen–detector distance. The aberration correction, $f(\varepsilon)$, is given in equation (36). Figs 12 and 13 show the effect of diffraction angle and specimen thickness.

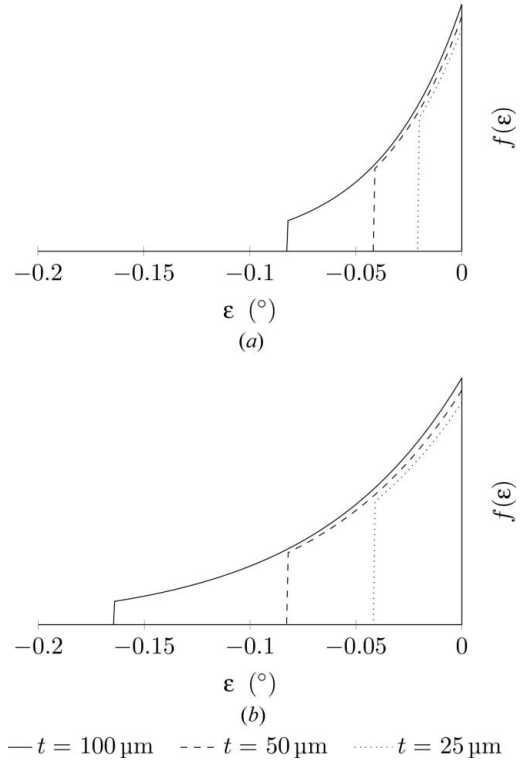

Figure 12
Normalized absorption profiles for a specimen in asymmetric transmission geometry at (*a*) 30 and (*b*) 90° 2θ, for a range of specimen thicknesses. The profiles have been scaled for clarity, as they are identical prior to the cutoff. These profiles are described by equation (36) with $\mu = 50\ \text{cm}^{-1}$, $\omega = 10°$ and $R_s = 200$ mm, and with $\beta = 180 - (2\theta + \omega)$.

$$w = \frac{b \sin\beta}{R_s \sin\omega} \frac{180}{\pi}, \tag{38}$$

where b is the beam height and R_s is the specimen–detector distance.

In order to model the peak shape resulting from this geometry, the absorption correction of equation (36) is convoluted with a hat function with a width given by equation (38). This approach has been validated against a ray-tracing model consisting of 10^5 points randomly placed in the area defined by the incident beam and specimen thickness. ε and intensity attenuation values were calculated for each point and then placed into ε bins of width 0.01°. Diffraction peaks were generated for a variety of μ, t_s, ω and β values and modelled in both *TOPAS* (Bruker, 2014) and *Maple* (Maplesoft, 2014). Fig. 14 shows the agreement between the model and ray-trace data for diffraction peaks at 30 and 90° 2θ for ω = 10°. The peaks are quite asymmetric, and the peak centroid is displaced from the true peak position, which will impact on all crystallographic parameters depending on peak position. Application of this physically derived peak shape through a fundamental parameters approach allows for the extraction of the true peak position.

2.2.3. Peak position corrections. The specimen displacement in this geometry (see Fig. 15) is again different from that of previous geometries. Assuming a small angle, then the peak offset in degrees due to a displacement, s, perpendicular to the specimen surface in asymmetric transmission is given by

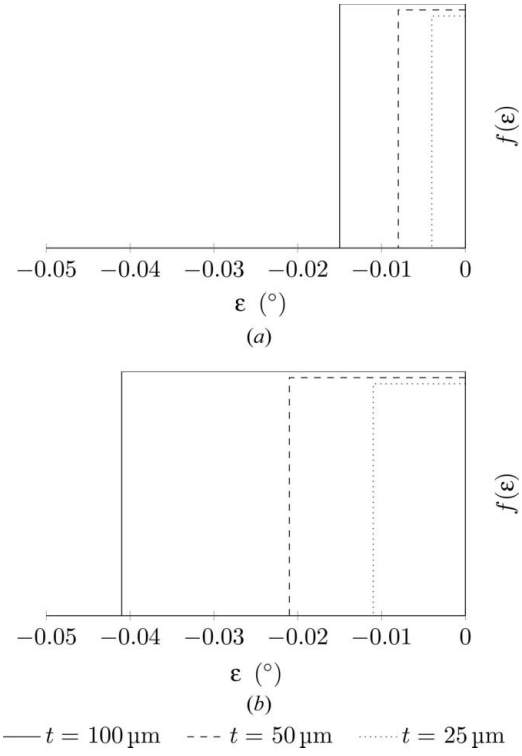

Figure 13
Normalized absorption profiles for a specimen in symmetric transmission geometry at (*a*) 30 and (*b*) 90° 2θ, for a range of specimen thicknesses. The profiles have been scaled for clarity, as they are identical prior to the cutoff. These profiles are described by equation (37) with R_s = 200 mm.

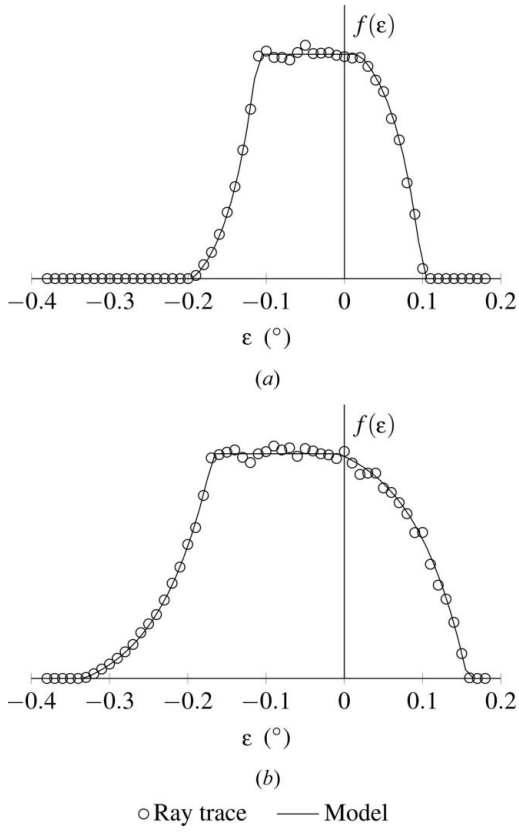

Figure 14
Ray tracing and model fits at (*a*) 30 and (*b*) 90° 2θ for a specimen in asymmetric transmission. The ray tracing data were calculated for a parallel incident beam of height 0.2 mm, with t_s = 0.1 mm, ω = 10°, μ = 50 cm^{-1} and R_s = 200 mm^{-1}. The models were constructed in *Maple* and consist of the absorption profile defined in equation (36) convoluted with a hat function with a width defined by equation (38). Note that the peak centroid is significantly displaced from the peak position.

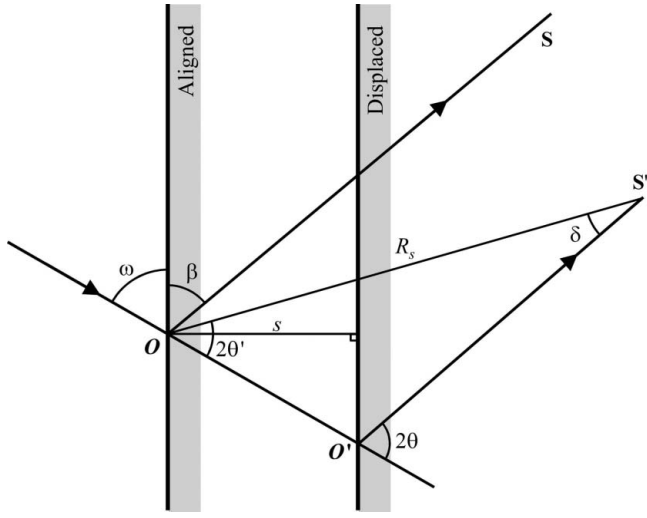

Figure 15
Geometrical argument for the specimen displacement correction for transmission geometry. The displacement causes a diffraction peak with an angle 2θ, which should be recorded at S, to be recorded at S', with a diffraction angle of $2\theta - \delta$. R_s is the specimen–detector distance. δ is given by equation (39).

$$\delta = \frac{s}{R_s}\frac{\sin 2\theta}{\sin \omega}\frac{180}{\pi}, \tag{39}$$

and in the case of symmetric transmission, the peak offset is given by

$$\delta = \frac{s}{R_s} 2 \sin\theta \frac{180}{\pi}. \tag{40}$$

2.3. Debye–Scherrer geometry

Intensity corrections and the peak shift due to absorption in the capillary, as well as an integral for calculating the peak profile for a parallel incident beam, are given by Sabine *et al.* (1998).

2.3.1. Peak intensity corrections. When modelling data in this geometry, the integrated intensities must be scaled by an absorption factor:

$$I_{\text{scale}} = A(\theta) = A_L \cos^2\theta + A_B \sin^2\theta. \tag{41}$$

Here, A_L and A_B are the absorption factors at the Laue (θ = 0°) and Bragg (θ = 90°) conditions and have the following exact analytical expressions (Dwiggins, 1972):

$$A_L = 2\left[I_0(z) - L_0(z) - \frac{I_1(z) - L_1(z)}{z}\right], \tag{42}$$

$$A_B = \frac{I_1(2z) - L_1(2z)}{z}, \tag{43}$$

where $z = 2\mu r$, r is the capillary radius, $I_v(z)$ is the vth-order modified Bessel function and $L_v(z)$ is the vth-order modified Struve function.

2.3.2. Peak profile corrections. Sabine *et al.* (1998) derived the peak profile for a capillary with a parallel incident beam as

$$f(y) = \begin{cases} (1/2)\int_{-(1-y^2)^{1/2}}^{(1-y^2)^{1/2}} \exp\left[-\mu(x_1 + x_2)\right] dz & -1 \le y \le 1 \\ 0 & \text{otherwise} \end{cases} \tag{44}$$

where x_1 and x_2 are the path lengths for the incident and diffracted beams, respectively, given by

$$x_1 = r\left\{z\cos 2\theta - y \sin 2\theta + \left[1 - (y\cos 2\theta + z \sin 2\theta)^2\right]^{1/2}\right\}, \tag{45}$$

$$x_2 = r\left[-z + (1 - y^2)^{1/2}\right], \tag{46}$$

and ε is given as

$$\varepsilon = \frac{yr}{R_s}\frac{180}{\pi}. \tag{47}$$

Here, r is the capillary radius and z, y are Cartesian coordinates of the point of diffraction and have a range of (−1, 1). How this profile arises is shown in Fig. 16. Fig. 17 shows

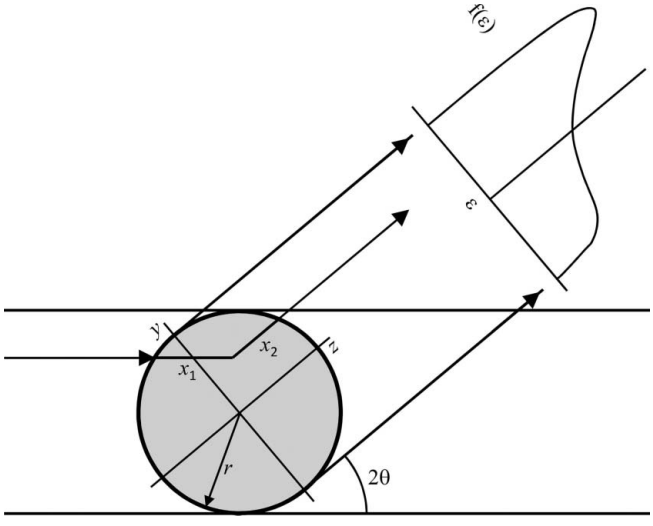

Figure 16
Geometry for the derivation of the peak shape profile for parallel incident beam capillary transmission (after Sabine *et al.*, 1998). The aberration correction, $f(\varepsilon)$, is given by equation (44). Fig. 17 shows the effect of diffraction angle and linear absorption coefficient.

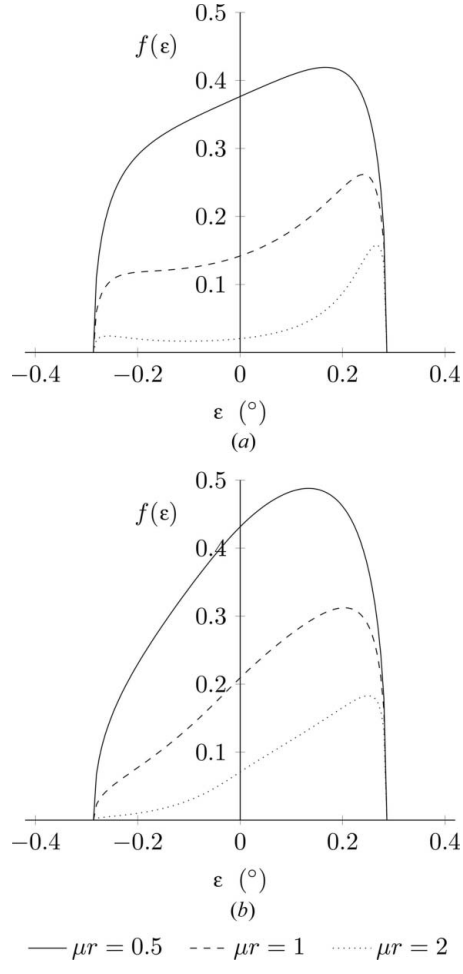

Figure 17
Peak shape and intensity profiles for a capillary specimen in Debye–Scherrer geometry at (*a*) 30 and (*b*) 90° 2θ, for a range of linear absorption coefficients. As the specimen becomes more absorbing, diffraction occurs preferentially from the outside of the capillary. These profiles are described by equation (44) with μ = 5, 10 and 20 cm^{-1}, r = 1 mm, and R_s = 200 mm.

profiles due to the capillary over a range of μr values at 30 and 90° 2θ.

2.3.3. Peak position corrections. Sabine *et al.* (1998) also took the position of the peak centroids and determined an empirical function to describe the shift in the peak position due to absorption in the range $0 < \mu r < 6$:

$$\delta = A\theta^{B}(90 - \theta)^{C}, \tag{48}$$

where θ is given in degrees and $A = 3.3\mu r \times 10^{-5}$, $B = 1.168 - 0.22\mu r + 0.0168(\mu r)^2$ and $C = 1.155 + 0.2054\mu r - 0.0224(\mu r)^2$. Application of the peak profile correction will account for this shift in peak position without the need for this correction.

Peaks may also shift because of incorrect alignment or segregation of the specimen inside the capillary (Scarlett *et al.*, 2010). Peak shift corrections for specimen displacements, s, parallel and perpendicular to the incident beam were derived by Scarlett *et al.* (2010) as

$$\delta = -\frac{s_{\parallel}}{R_s}\sin 2\theta\frac{180}{\pi}, \tag{49}$$

$$\delta = \frac{s_{\perp}}{R_s}\cos 2\theta\frac{180}{\pi}, \tag{50}$$

where the specimen–detector distance is R_s. Both equations may be used simultaneously to describe any off-axis displacement, given a sufficient 2θ range to define both displacements.

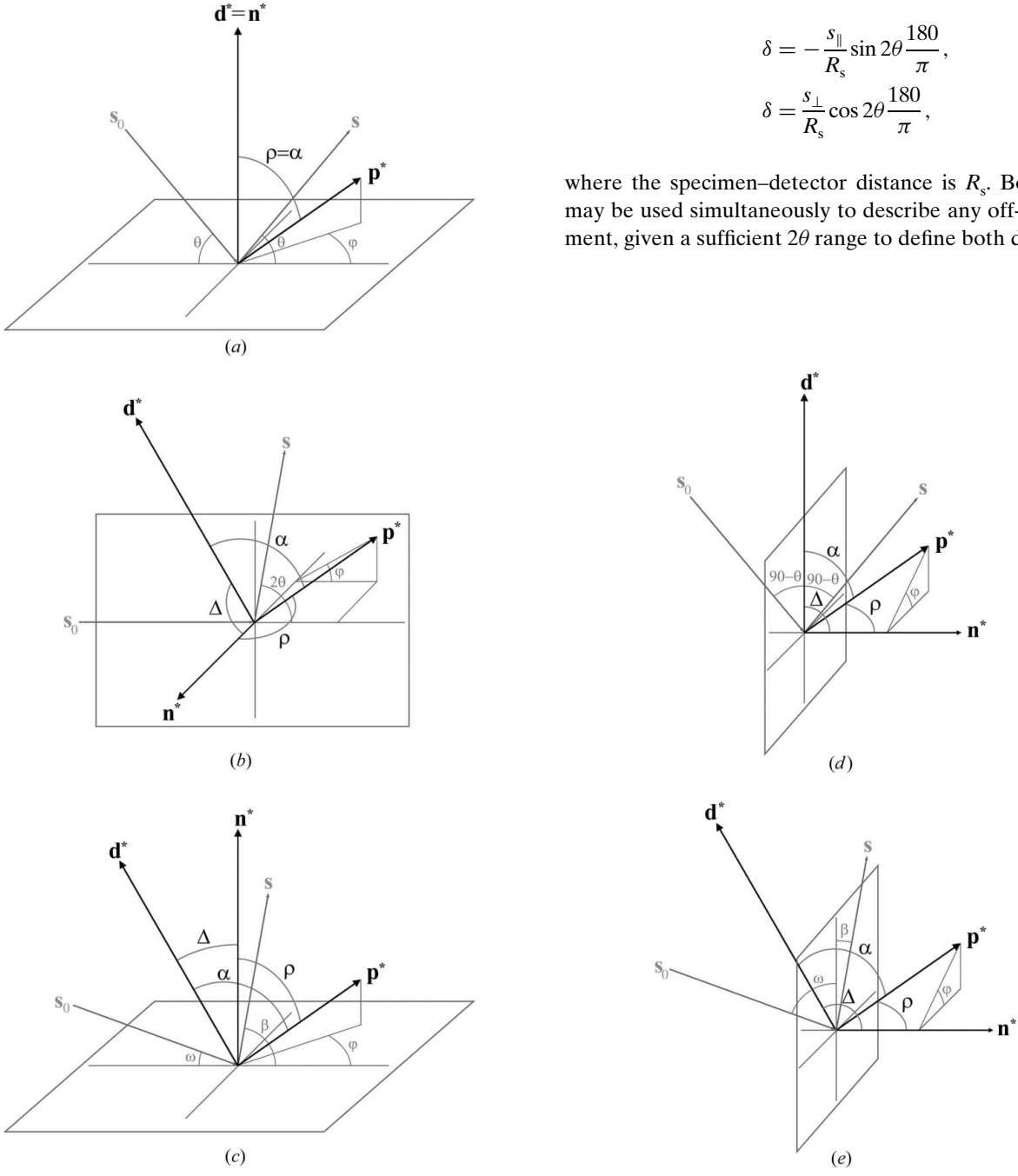

Figure 18
Required vectors and angles for both March–Dollase and spherical harmonics corrections for (*a*) symmetric reflection, (*b*) Debye–Scherrer, (*c*) asymmetric reflection, (*d*) symmetric transmission and (*e*) asymmetric transmission geometries. $\mathbf{d}^*$ is the diffraction vector, $\mathbf{n}^*$ is the rotation axis of the specimen and $\mathbf{p}^*$ is the preferred orientation vector. The angle between $\mathbf{d}^*$ and $\mathbf{n}^*$ is Δ, $\mathbf{d}^*$ and $\mathbf{p}^*$ is α, and $\mathbf{n}^*$ and $\mathbf{p}^*$ is ρ. φ is the rotation angle about $\mathbf{n}^*$ of the projection of $\mathbf{p}^*$ onto the plane defined by $\mathbf{n}^*$. $\mathbf{s}_0$ and $\mathbf{s}$ are the incident and diffracted beams, respectively.

3. Preferred orientation corrections

The diffraction geometry can have subtle effects on phase-specific corrections, such as preferred orientation. The March–Dollase correction for preferred orientation (Dollase, 1986) is given by

$$P_{\rm MD} = \left(r^2 \cos^2 \rho + \frac{\sin^2 \rho}{r}\right)^{-3/2}. \quad (51)$$

Here, ρ is the angle between the preferred orientation direction ($\mathbf{p}^*$) and the specimen normal ($\mathbf{n}^*$), which is taken to be the direction of the specimen's rotational symmetry, and r is a measure of the degree of orientation, where $r = 1$ is a random powder. In symmetric reflection geometry, the specimen normal and the diffraction vector ($\mathbf{d}^*$) are parallel, which allows ρ to be given simply as α, the angle between $\mathbf{d}^*$ and $\mathbf{p}^*$, simplifying the calculations (see Fig. 18*a*).

If the symmetric reflection implementation of the March–Dollase preferred orientation correction is applied directly to data collected in Debye–Scherrer geometry, this results in the preferred orientation factor, r, being approximated as $r^{-1/2}$, but only for values close to unity (Howard & Kisi, 2000). As the powder becomes progressively more oriented, this approximation becomes significantly worse. The Debye–Scherrer geometry, with respect to preferred orientation corrections, is shown in Fig. 18(*b*), where the specimen normal is at right angles to the diffraction vector. Application of the March–Dollase correction, as is, to asymmetric reflection is incorrect, as the angles between $\mathbf{d}^*$, $\mathbf{n}^*$ and $\mathbf{p}^*$ are continuously changing (see Fig. 18*c*). The relevant geometry for symmetric and asymmetric transmission is shown in Figs. 18(*d*) and 18(*e*). It can be seen how the geometry is similar to that of Debye–Scherrer and asymmetric reflection.

Ida (2013) comprehensively covers the application of the March–Dollase model to asymmetric reflection and Debye–Scherrer geometries, and shows that a simple implementation of the preferred orientation correction, f, can be given by

$$f(r, \alpha, \Delta) = \frac{1}{2\pi} \int_0^{2\pi} g(r, \alpha, \Delta, \varphi)\, {\rm d}\varphi, \quad (52)$$

$$g(r, \alpha, \Delta, \varphi) = P_{\rm MD}, \quad (53)$$

$$\cos \rho = \cos \alpha \cos \Delta - \sin \alpha \sin \Delta \sin \varphi, \quad (54)$$

where ρ is the angle between $\mathbf{n}^*$ and $\mathbf{p}^*$, α is the angle between $\mathbf{d}^*$ and $\mathbf{p}^*$, Δ is the angle between $\mathbf{d}^*$ and $\mathbf{n}^*$, and φ is the rotation angle about $\mathbf{n}^*$ of the projection of $\mathbf{p}^*$ onto the plane defined by $\mathbf{n}^*$ (see Fig. 18). As a first approximation, equation (3) can replaced by a sum,

$$f(r, \alpha, \Delta) \simeq \frac{1}{N} \sum_{j=0}^{N-1} g\left[r, \alpha, \Delta, \frac{j - (1/2)}{N}\pi\right], \quad (55)$$

where $N = 16$ is appropriate for most applications, as shown by Ida (2013). If $r \gg 1$, this summation approach breaks down, and the other, more rigorous, approaches outlined by Ida should be applied. However, if r moves too far from unity, then the March–Dollase correction itself is also probably not an appropriate model (Ida, 2013).

The same alteration is also relevant to the use of spherical harmonics (Järvinen, 1993), where the intensity correction is given by

$$\overline{W}(hkl, \Delta) = \sum_{ij} C_{ij} Y_{ij}(\theta_{hkl}, \varphi_{hkl}) P_i(\cos \Delta). \quad (56)$$

C_{ij} are adjustable parameters, Y_{ij} are the symmetrized spherical harmonics, Δ is the angle between $\mathbf{d}^*$ and $\mathbf{n}^*$, and $P_i(x)$ is the ith-order Legendre polynomial. In symmetric reflection, $\Delta = 0^\circ$ 2θ, and all of the associated Legendre polynomials have a value of 1 and as such do not influence the correction. In Debye–Scherrer, asymmetric reflection, asymmetric transmission and symmetric transmission geometries, Δ has values of 90°, $\theta - \omega$, $\theta + \omega$ and 90°, respectively, and so these angles must be included in the Legendre polynomials in order to obtain representative corrections.

As with any preferred orientation corrections, it is almost always better to carry out a texture analysis to properly quantify the orientation present in the specimen (Lutterotti *et al.*, 2004), but this is not often appropriate for *in situ* studies. With these corrections, the approximate model is being applied exactly in the new geometries, which discounts any effect an incorrect implementation may have on an analysis.

4. Implementation

The corrections outlined in this paper have been implemented in the *TOPAS* (Bruker, 2014) macro language and are available in the supporting information and on the *TOPAS* wiki (Evans, 2010, 2015). The Sabine corrections for capillary specimens are already implemented in the base installation of *TOPAS*, and there are also capillary profile corrections available for parallel and divergent beam optics.

5. Conclusions

The aberration corrections outlined in this paper form an important basis in the modelling of diffraction data collected in non-Bragg–Brentano geometries. The common factor between all of these corrections is a careful analysis of the geometry of the experiment, resulting in derivations of peak intensity, profile and displacement equations which allow a fundamental parameters approach to the modelling of aberrations present in data collected in different geometries. The implementation of such physically realistic models allows data taken from different instruments in different geometries to be compared directly, without having to take into account differences due to the vagaries of the data collection.

References

Bruker (2014). *Topas*. Version 5. Bruker AXS, Karlsruhe, Germany.
Cheary, R. W. & Coelho, A. (1992). *J. Appl. Cryst.* **25**, 109–121.
Cheary, R. W. & Coelho, A. A. (1998*a*). *J. Appl. Cryst.* **31**, 851–861.
Cheary, R. W. & Coelho, A. A. (1998*b*). *J. Appl. Cryst.* **31**, 862–868.

Cheary, R. W., Coelho, A. A. & Cline, J. P. (2004). *J. Res. Natl Inst. Stand. Technol.* **109**, 1–25.
Dollase, W. A. (1986). *J. Appl. Cryst.* **19**, 267–272.
Dwiggins, C. W. (1972). *Acta Cryst.* A**28**, 219–220.
Egami, T. & Billinge, S. J. L. (2003). *Underneath the Bragg Peaks: Structural Analysis of Complex Materials*. Amsterdam: Pergamon.
Evans, J. S. O. (2010). *Mater. Sci. Forum*, **651**, 1–9.
Evans, J. S. O. (2015). *Topas Wiki*, http://topas.dur.ac.uk/topaswiki/doku.php.
Finger, L. W., Cox, D. E. & Jephcoat, A. P. (1994). *J. Appl. Cryst.* **27**, 892–900.
Howard, C. J. & Kisi, E. H. (2000). *J. Appl. Cryst.* **33**, 1434–1435.
Ida, T. (2013). *Annu. Rep. Adv. Ceram. Res. Cent. Nagoya Inst. Technol.* **2**, 7–11.
Järvinen, M. (1993). *J. Appl. Cryst.* **26**, 525–531.
Klug, H. P. & Alexander, L. E. (1974). *X-ray Diffraction Procedures for Polycrystalline and Amorphous Materials*, 2nd ed. New York: John Wiley and Sons.
Laar, B. van & Yelon, W. B. (1984). *J. Appl. Cryst.* **17**, 47–54.
Lutterotti, L., Chateigner, D., Ferrari, S. & Ricote, J. (2004). *Thin Solid Films*, **450**, 34–41.
Maplesoft (2014). *Maple.* Version 18. Maplesoft, Waterloo, Ontario, Canada.
Masson, O., Guinebretière, R. & Dauger, A. (1996). *J. Appl. Cryst.* **29**, 540–546.
Rietveld, H. M. (1969). *J. Appl. Cryst.* **2**, 65–71.
Rowles, M. R. & Madsen, I. C. (2010). *J. Appl. Cryst.* **43**, 632–634.
Sabine, T. M., Hunter, B. A., Sabine, W. R. & Ball, C. J. (1998). *J. Appl. Cryst.* **31**, 47–51.
Scarlett, N. V. Y., Rowles, M. R., Wallwork, K. S. & Madsen, I. C. (2011). *J. Appl. Cryst.* **44**, 60–64.
Schmitt, B., Brönnimann, C., Eikenberry, E. F., Gozzo, F., Hörmann, C., Horisberger, R. & Patterson, B. (2003). *Nucl. Instrum. Methods Phys. Res. Sect. A*, **501**, 267–272.
Toraya, H., Huang, T. C. & Wu, Y. (1993). *J. Appl. Cryst.* **26**, 774–777.
Zevin, L. S. & Kimmel, G. (1995). *Quantitative X-ray Diffractometry.* New York: Springer.